



Graphene based heterostructures

C. Dean^{a,b,*}, A.F. Young^c, L. Wang^a, I. Meric^b, G.-H. Lee^a, K. Watanabe^d, T. Taniguchi^d, K. Shepard^b, P. Kim^c, J. Hone^a

^a Department of Mechanical Engineering, Columbia University, New York, NY 10027, USA

^b Department of Electrical Engineering, Columbia University, New York, NY 10027, USA

^c Department of Physics, Columbia University, New York, NY 10027, USA

^d Advanced Materials Laboratory, National Institute for Materials Science, 1-1 Namiki, Tsukuba 305-0044, Japan

ARTICLE INFO

Article history:

Accepted 12 April 2012

by L. Brey

Available online 10 May 2012

Keywords:

A. Graphene

A. Hexagonal boron nitride

C. Heterostructures

D. Quantum Hall effect

D. Landau level splitting

ABSTRACT

The two dimensional charge carriers in monolayer and bilayer graphene are described by massless and massive chiral Dirac Hamiltonians, respectively. These two-dimensional materials are predicted to exhibit a wide range of behavior, etc. However, graphene devices on a typical three-dimensional insulating substrates such as SiO₂ are highly disordered, exhibiting characteristics that are far inferior to the expected intrinsic properties of graphene. We have developed a novel technique for substrate engineering of graphene devices using layered dielectric materials to build graphene based vertical heterostructures. We employ hBN, an insulating isomorph of graphite, as a substrate and gate dielectric for graphene electronics. In this review, we describe the fabrication and characterization of high-quality exfoliated mono- and bilayer graphene devices on single-crystal hBN substrates, using a mechanical transfer process. Graphene devices on hBN substrates have mobilities and carrier inhomogeneities that are almost an order of magnitude better than devices on SiO₂. We use the enhanced mobility of electrons in hBN supported graphene to investigate the effects of electronic interactions. We find that interactions drive spontaneous breaking of the emergent SU(4) symmetry of the graphene Landau levels, leading to a variety of non-trivial integer and fractional quantum Hall states. The ability to assemble crystalline layered materials in a controlled way permits the fabrication of graphene devices on other promising dielectrics and allows for the realization of more complex graphene heterostructures.

© 2012 Elsevier Ltd. All rights reserved.

1. Introduction

Improving the quality of graphene samples is required to fully understand and utilize the exceptional electronic properties of this novel two-dimensional (2D) material. It is now well understood that the quality of graphene on SiO₂ is limited by scattering from charged surface states and impurities [1], substrate surface roughness [2,3] and SiO₂ surface optical phonons [4,5]. Furthermore, near charge neutrality, substrate-induced disorder creates inhomogeneous patterns of electron and hole puddles [6–8]. While suspending the graphene above the substrate leads to a substantial improvement in device quality [9,10], this geometry imposes severe limitations on device architecture and functionality. There has been a growing need, therefore, to identify dielectrics that allow at the functionality of a substrate-supported geometry while retaining the quality achieved with suspended

samples. Other three-dimensional insulating substrates that have been examined also display the same surface induced effects that limit carrier mobility [11,12].

Hexagonal boron nitride (hBN) is an appealing substrate dielectric for use in improved graphene-based devices. hBN is an insulating isomorph of graphite with boron and nitrogen atoms occupying the inequivalent A and B sublattices in the Bernal structure. The different on-site energies of the boron and nitrogen atoms result in a large (5.97 eV) bandgap [13] and a small (1.7%) lattice mismatch with graphite [14]. Owing to the strong, in-plane, ionic bonding of the planar hexagonal lattice structure, hBN is relatively inert and is expected to be free of dangling bonds or surface charge traps. Furthermore, the atomically planar surface should suppress rippling in graphene, which has been shown to mechanically conform to both corrugated and flat substrates [2,15]. The dielectric properties of hBN are similar to those of SiO₂, allowing the use of hBN as an alternative gate dielectric with no loss of functionality [16]. Moreover, the surface optical phonon modes of hBN have energies two times larger than similar modes in SiO₂, suggesting the possibility of an improved high-temperature and high-electric-field performance of hBN

* Corresponding author at: Department of Mechanical Engineering, Columbia University, New York, NY 10027, USA.

E-mail address: jh2228@columbia.edu (C. Dean).

based graphene devices over those using typical oxide/graphene stacks [17,18].

In this paper, we review the fabrication and characterization of high-quality graphene hBN vertical heterostructures. We will first describe the fabrication methods of creating vertical stacks of mono- and bilayer graphene devices on single-crystal hBN substrates, using a mechanical transfer process. We then present the characterization of the quality of 2D dielectric hBN and conducting graphene. Finally we will summarize the new physics we find in graphene/hBN structures, by presenting the experimental observation of interactions driven, broken SU(4) symmetry integer and fractional quantum Hall states.

2. Fabrication of graphene hBN heterostructures

We use a co-laminating and restacking method to construct graphene–hBN heterostacks, as depicted in Fig. 1. Fabrication begins with the mechanical exfoliation of hBN single crystals onto silicon wafers coated in 285 nm thermal oxide. The hBN flakes used in this study are exfoliated from ultra-pure, hexagonal-BN single crystals, grown by the method described in Ref. [19]. Graphene is exfoliated separately onto a polymer stack consisting of PMMA (molecular weight 495 K, thickness 275 nm) on top of a water-soluble layer, either Mitsubishi Rayon aqua-SAVE or poly-vinyl alcohol. All of the thin-film liftoff based transfer methods rely on the same optical Fabry–Perot interference responsible for the original isolation of graphene on SiO₂ [20]. The optical contrast on SiO₂ is sufficient to identify hBN flakes with thicknesses down to a single monolayer [21]. Likewise, graphene down to monolayer thickness can be imaged on polymer layers of suitable thickness. We employ a band pass filter ($\lambda 562 \pm 20$ nm) between the eyepiece and microscope objective, to maximize contrast. The polymer stack is tuned to provide high contrast for monolayer graphene, but also works for thin hBN or other exfoliatable materials. The graphene layer thickness is occasionally verified by Raman spectroscopy before transfer, although this is generally unnecessary for substrates with properly tuned optical thickness.

After the graphene is exfoliated and suitable flakes are identified by optical microscopy, DI water is used to dissolve the bottom polymer layer, leaving the hydrophobic PMMA with graphene floating on top of the water bath. The PMMA membrane is then inverted and adhered to a glass transfer slide, which is clamped onto the arm of a micromanipulator mounted on an optical microscope on a standard wafer probe station. The microscope is used to optically locate the position of the graphene flake on the suspended polymer film, and precisely align the

graphene to the target BN, after which the two layers are brought into contact. With this technique, the graphene can be positioned to within a few microns of the target position. During transfer, the target substrate is heated to 105 °C in order to drive off water adsorbed on the surface of the graphene or hBN flakes. Once the PMMA film is observed to touch the wafer surface, the substrate is heated to 120 °C to soften the PMMA so that it adheres to the substrate (d). The manipulator is then lifted to leave the PMMA film and graphene on the substrate. Once transferred, the PMMA is dissolved in acetone (e). Fig. 2 shows an optical micrograph of a graphene flake transferred onto hBN. Finally, samples are annealed in flowing H₂/Ar gas at 340 °C for 3 h to remove resist residue, and then examined by AFM.

Fig. 3 shows AFM images of graphene transferred to hBN, acquired in air using a standard silicon cantilever in tapping mode. On the scale of the entire flake (a), it can be seen that the transfer process is not perfect: there are a number of folds and bubbles in the graphene layer. Although the above annealing process can reduce the size and frequency of these features, it does not completely eliminate them. However, it can also be clearly seen that there exist large (up to ~ 10 μ m) areas in which the graphene is flat and lacking in any imperfections. All of the devices described below are fabricated from these pre-selected areas. Fig. 3(b) shows a high-resolution scan of a

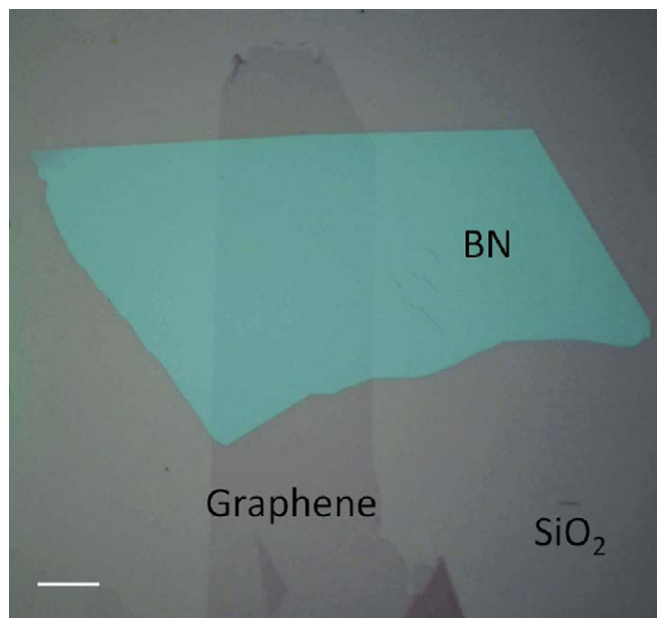


Fig. 2. (Color online) Transferred graphene on hBN. Optical micrograph of large graphene flake transferred onto a 23 nm thick hBN crystal. Scale bar 10 μ m.

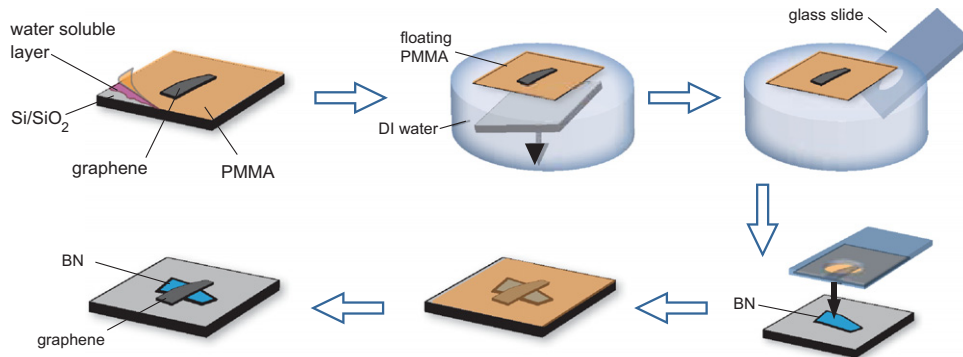


Fig. 1. (Color online) Mechanical transfer process. (a) Graphene exfoliated onto polymer stack. (b) PMMA with graphene floating on water bath. (c) PMMA membrane inverted and attached to the micromanipulator stage, then aligned above an exfoliated hBN flake. (d) Membrane and graphene transferred to the substrate. (e) Graphene on hBN after PMMA removal.

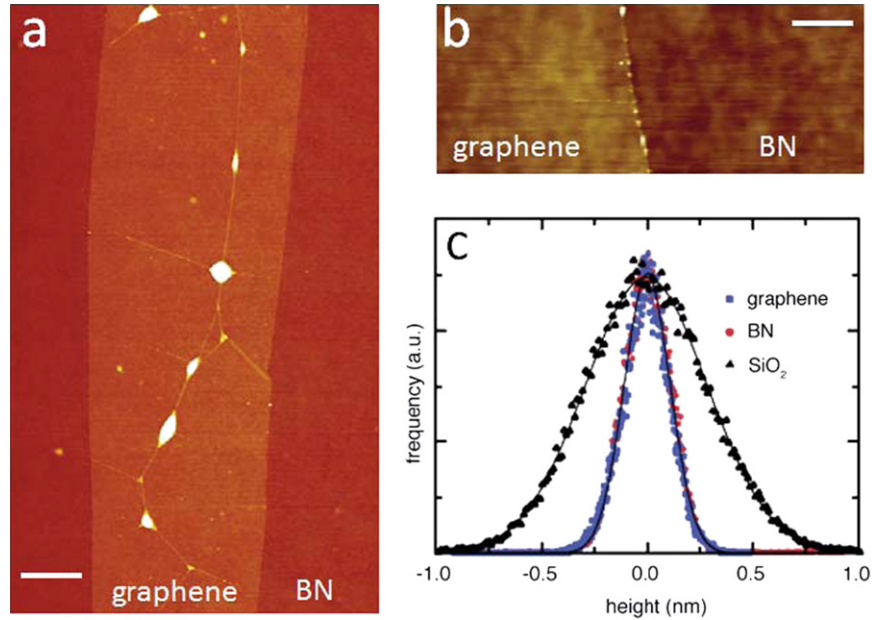


Fig. 3. (Color online) Mechanical characterization of hBN flakes. (a) AFM topographic image of a graphene flake transferred onto hBN. Scale bar 5 μm . (b) AFM image of a smaller, flat area at the edge of the graphene flake. Scale bar 200 nm. (c) Height histogram of the hBN and graphene surfaces, compared to the surface of SiO₂.

flat area at the edge of a graphene flake on hBN. Both the graphene and hBN surfaces appear completely devoid of any features on this scale. Fig. 3c shows a histogram of the measured surface roughness for both the graphene and the hBN, acquired over a 300 nm² scan window. For hBN flakes thicker than ~ 5 nm, the hBN surface roughness approaches that of pristine HOPG (~ 70 pm). Moreover, the graphene lying on the hBN has an identical roughness. Subsequent STM studies by other groups have improved the resolution of the roughness measurement, yielding a maximum roughness of ~ 30 -pm for both hBN and graphene on hBN [22]. We conclude that the graphene membrane conforms to the atomically flat hBN, consistent with the previous reports on both rippled [2] and flat [15] surfaces.

3. Tunneling and dielectric breakdown of hBN

We have characterized electronic tunneling and dielectric breakdown of hBN by conductive AFM [18] on gold-coated mica. Fig. 4(a) and (b) shows topography and conductance AFM images of hBN flakes with different thicknesses under a tip bias of 1 V. The tunneling current is a function of thickness, as expected, and is uniform within areas of the same thickness, confirming that the hBN crystals are electrically uniform.

Fig. 5 shows the tunneling conductance as a function of tip bias of multiple samples with different thicknesses. Low-bias direct tunneling is observed in mono-, bi-, and tri-layer hBN. For all thicknesses, Fowler–Nordheim tunneling (FNT) occurs at high bias, with an increase of breakdown voltage with thickness. The breakdown voltage increases linearly with thickness as $V=0.79$ V/nm, comparable to SiO₂. The direct-tunneling conductance decreases exponentially with thickness. This data indicates that it should be possible to use few-layer hBN as an atomically precise tunnel barrier.

4. Transport characterization of hBN supported graphene devices

For the measurement of transport properties, electrical leads are deposited using standard electron beam lithography

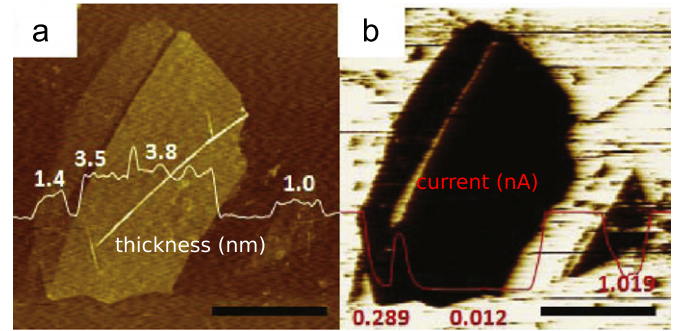


Fig. 4. (Color online) Conducting AFM of BN on gold-coated mica. (a) Topographic image. The line indicates the thickness in nm along the section indicated by the dashed line. (b) Conductance image with a tip bias of 1 V. The line indicates the tunneling current, in nA. Scale bars are 5 μm .

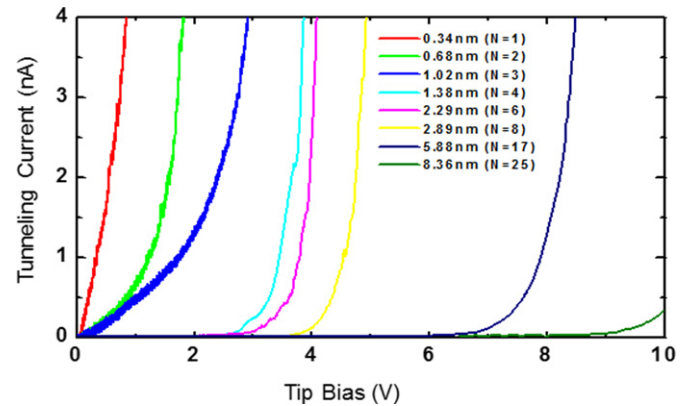


Fig. 5. (Color online) Electron tunneling through BN. Tunneling current versus tip bias, for samples of various thicknesses.

and lift-off. A second lithography step, followed by oxygen plasma etching, is used to shape the graphene into Hall bar structures, with typical channel length and width of ≈ 1 μm . Following these steps, the samples are typically annealed for a second time in flowing H₂/Ar gas at 340 $^{\circ}\text{C}$ for 3 h to remove resist residue. The

devices presented in the main text did not undergo any further treatment (i.e. in situ vacuum annealing, etc.) after removal from the H_2/Ar . Fig. 6 shows an SEM image of a completed device. For the analysis below, we take the channel length as the shortest distance between the voltage probes, for the most conservative estimate of device resistance. The capacitive coupling to the device is calculated by a standard parallel-plate formula, and checked by Hall effect measurements.

Fig. 7 shows the electrical transport measurements of typical monolayer and bilayer graphene samples on hBN at zero magnetic field. Fig. 7a shows four-probe resistivity of a typical monolayer graphene sample on hBN as a function of applied back gate voltage V_g . The resistivity peak, corresponding to the overall

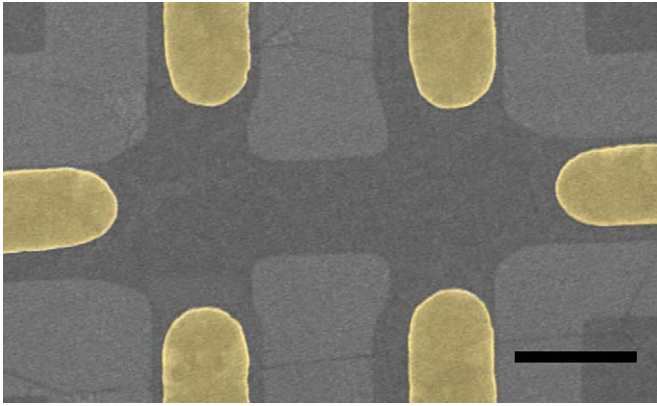


Fig. 6. (Color online) Device geometry. Scanning electron micrograph of Hall bar device. The graphene channel is the dark area spanning the electrodes (false-colored gold). Scale bar 1 μm .

charge neutrality point, is extremely narrow and typically occurs at nearly zero gate voltage. A resistivity curve for the same graphene flake on SiO_2 is shown for comparison. This curve, typical for such samples, shows a broader peak and a large offset from zero. Fig. 7b shows the conductivity of the hBN-supported sample versus gate voltage. The conductivity is strongly sublinear in carrier density, indicating a crossover from scattering dominated by charge impurities at low density to short-range impurity scattering at large carrier density [23,6,7,3,24]. The data is well fit (dashed line) by a self-consistent Boltzmann equation for diffusive transport that includes both long and short range scattering [6,7], $\sigma^{-1} = (ne\mu_C + \sigma_0)^{-1} + \rho_s$, where μ_C is the density-independent mobility due to charged-impurity Coulomb (long-range) scattering, ρ_s is the contribution to resistivity from short-range scattering, and σ_0 is the residual conductivity at the charge neutrality point. The device shown has $\mu_C \sim 60,000 \text{ cm}^2/\text{Vs}$, larger than the best value seen on SiO_2 , and $\rho_s \sim 71 \Omega$, which is similar to values obtained on SiO_2 . These values indicate a decrease charged impurity scattering, but a similar degree of short range scattering, in comparison to the best SiO_2 samples. The similar value of ρ_s observed for SiO_2 and hBN supported-graphene samples tends to rule out scattering off ripples and out-of-plane vibrations [3,25] as a dominant source of short-range scattering, since these should be suppressed on atomically flat hBN.

The width of the resistivity peak at the charge neutrality point is $\sim 1 \text{ V}$, giving an upper bound for disorder-induced carrier density fluctuation of $\delta n < 7 \times 10^{10} \text{ cm}^{-2}$, a factor of ~ 3 improvement over SiO_2 -supported samples [8]. An alternate estimate of this inhomogeneity is obtained from the temperature dependence of the minimum conductivity. In Fig. 7c, σ_{\min} increases by a factor of two between 4 K and 200 K. Whereas on SiO_2 σ_{\min} typically exhibits $< 30\%$ variation in the same range [9]. σ_{\min} is expected to vary with temperature only for $k_B T > E_{\text{puddle}}$ where for monolayer graphene [9]

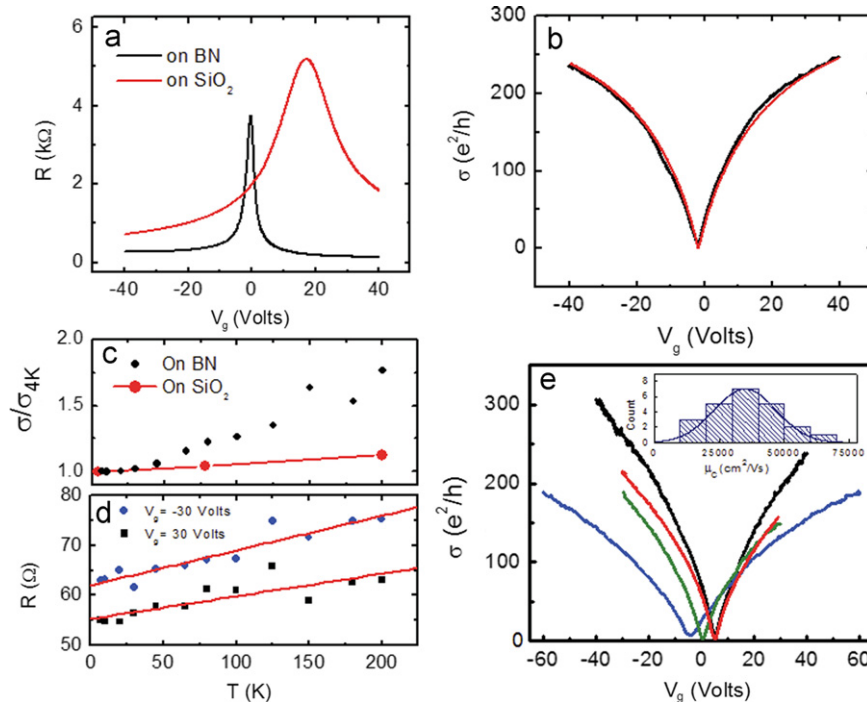


Fig. 7. (Color online) Transport characterization. (a) Resistance versus back gate voltage for typical monolayer graphene devices on hBN and on SiO_2 . (b) Conductivity versus charge density for hBN-supported device (red line), and fit to the data (black dashed line). (c) Minimum conductivity at the charge neutrality point, as a function of temperature, normalized to the value at 4 K, for hBN and SiO_2 -supported devices. (d) Resistivity at high charge density as a function of temperature. (e) Conductivity curves for four representative devices. The inset shows the statistical distribution of the derived density-independent mobility.

$E_{\text{pudde}} \approx \hbar v_f \sqrt{\pi \delta n}$. Here σ_{min} saturates to $\sim 6e^2/h$ for $T \lesssim 15$ K giving an upper bound of $\delta n \sim 10^9 \text{ cm}^{-2}$. The δn estimated by these two measures is consistent with similar analysis performed on suspended devices [9,26].

The temperature dependence of the resistivity at high density is shown in Fig. 7d. The high-density resistance increases linearly with temperature due to longitudinal acoustic phonon scattering, $\rho_{\text{LA}}(T) = (\hbar/e^2)(\pi^2 D_A^2 k_B T / 2 \hbar^2 \rho_s v_s^2 v_f^2)$, where $\rho_s = 7.6 \times 10^{-7} \text{ kg/m}^2$ is the graphene mass density, $v_f = 1 \times 10^6 \text{ m/s}$ is the Fermi velocity, $v_s = 2 \times 10^4 \text{ m/s}$ is the longitudinal acoustic phonon velocity and D_A is the acoustic deformation potential [5,9]. Linear fits to the electron (hole) branches give $D_A \sim 18 \text{ eV}$ ($D_A \sim 21 \text{ eV}$), in agreement with previous measurements [5,9,3,24]. No indication of activated remote surface phonon scattering is seen up to 200 K.

Conductance curves that represent the statistical variation of the performance of hBN-supported graphene are shown in Fig. 7e. All of the devices show high mobility and a charge neutrality point near zero gate voltage. Interestingly, the device mobility does not seem to be correlated with the position of the Dirac peak, indicating that the amount of charged-impurity scattering is not directly proportional to the amount of static charge trapped at the SiO_2 –hBN interface. The inset shows a histogram of the derived charged-impurity mobility of 23 devices. The mean value of μ_C is $\sim 35,000 \text{ cm}^2/\text{V s}$.

5. Magnetotransport measurements

Magnetotransport measurements provide further confirmation of the high material quality achieved in these samples. Fig. 8a shows the magnetoconductivity σ_{xx} and Hall conductivity σ_{xy} as a function of density at $B = 14 \text{ T}$ for monolayer graphene, derived from the simultaneous measurement of magnetoresistance R_{xx} and Hall resistance R_{xy} in the Hall bar geometry shown in Fig. 6. Complete lifting of the four-fold degeneracy [27] of the zero energy Landau level is observed, with the additional quantum Hall states at $\nu = 0, +1, \pm 2$ exhibiting quantized Hall conductance $\sigma_{xy} = \nu e^2/h$ together with vanishing σ_{xx} . The dashed line in Fig. 8a indicates that the signatures of the $\nu = \pm 1$ quantum Hall effect (QHE) are visible at fields as low as $B = 8.5 \text{ T}$, more than a factor of two smaller than reported for monolayer graphene on SiO_2 [27].

A complete sequence of broken symmetry Landau levels are visible in bilayer graphene at $B = 14 \text{ T}$ (Fig. 8b). In our device, the substrate supported geometry allows us to probe much higher density than possible in suspended devices of similar quality [26]. Quantized Hall resistance is observed at $R_{xy} = (1/\nu)\hbar/e^2$ concomitant with minima in R_{xx} for all integer filling factors from $\nu = 1$ to at least $\nu = 16$. Density sweeps at lower fields show that the lifting of the expected four-fold degeneracy in bilayer graphene [26] is observable up to at least the fifth Landau level at less than 5 T . Complete quantization of the four-fold degenerate Landau levels and Shubnikov–de Haas oscillations is seen down to 2 and 0.4 T respectively (Fig. 8b).

Fig. 9a shows an enlargement of the magneto-transport measured from BLG on hBN presented in Fig. 8. Landau levels are labeled between 5 and 14 T , indicating that appearance of the four-fold symmetry breaking is visible down to approximately 5 T . Complete quantization of the four-fold degenerate LL's, evidenced by both quantization in R_{xy} and a near-zero minimum in R_{xx} , is observed down to approximately 2 T . The inset of Fig. 9a shows the low field Shubnikov–de Haas oscillations, which are visible down to as low as 0.4 T .

Magnetoresistance measured at fixed field and varying back-gate voltage are shown for several different fields in Fig. 9b. Minima in between the otherwise four-fold degenerate LL's, for LL index greater than $\nu = 4$, begin to emerge at $\sim 5 \text{ T}$, becoming fully

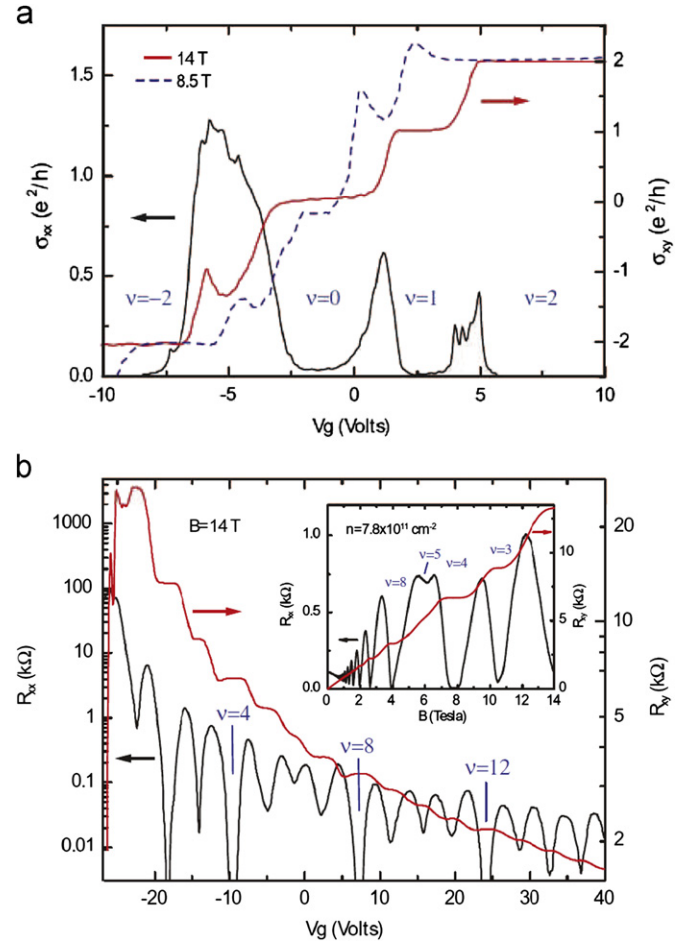


Fig. 8. (Color online) Magnetotransport of graphene on hBN devices. (a) Longitudinal and Hall conductivity versus gate voltage at $B = 14 \text{ T}$ (solid line) and 8.5 T (dashed line) for monolayer graphene. (b) Longitudinal and Hall resistance versus gate voltage at $B = 14 \text{ T}$ for bilayer graphene. Inset shows a magnetic field sweep at fixed density. SdH oscillations begin at $\sim 0.4 \text{ T}$ with Landau level symmetry breaking appearing at fields less than 6 T . $T \sim 2 \text{ K}$ in both panels.

quantized for all integer fillings up to at least $\nu = 20$ at 14 T . In the lowest energy LL, where the $n=0$ and $n=1$ levels are doubly degenerate, the $\nu = 2$ quantum Hall state shows a deep broad minimum at fields well below 5 T .

In the lowest Landau level the even-integer, $\nu = 2$, quantum Hall state has a larger gap compared to the odd-integer states, $\nu = 1$ and 3 , as judged by the depth of the R_{xx} minimum [26,28]. In the second Landau level, the situation is reversed, with the even integer state ($\nu = 6$) weaker than the odd integers ($\nu = 5, 7$). A full understanding of symmetry breaking with increasing Landau level index in bilayer graphene is postponed to the next section, where controllably applying a symmetry breaking field reveals the spin- and valley splitting of the LLs.

The technology of transferring atomically thin membranes from substrate to substrate while maintaining the integrity of the graphene and the quality of the electronic system opens up a number of experimental directions which were not possible before. Fig. 10 shows a few of the possible geometries for both technological and fundamental applications. In addition, the aligned transfer process can be easily extended to other materials amenable to mechanical exfoliation onto the polymer stack, including not only the family of graphenes but also MoS_2 , Niobium selenide, and cuprate superconductors of the BaSrCaCuO family.

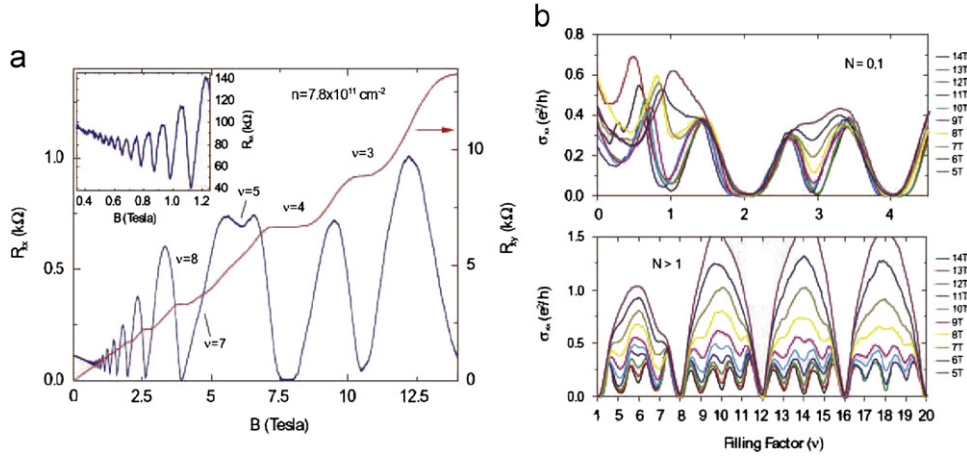


Fig. 9. (Color online) Additional magnetotransport data from a bilayer graphene on hBN sample. (a) Magnetoresistance (blue curve) and Hall resistance (red curve) versus B field of the BLG sample on hBN. $T \sim 4$ K and $n = 7.8 \times 10^{11} \text{ cm}^{-2}$. Landau levels between 5 and 14 T are labeled. Inset shows low field SdH oscillations, measured under the same conditions. (b) Magnetoresistance versus gate voltage of the same sample. Upper panel shows symmetry breaking in the lowest energy Landau level (i.e. $|\nu| < 4$). Lower panel shows symmetry breaking of the higher order Landau levels. The data is plotted versus filling factor for easier comparisons between different magnetic fields.

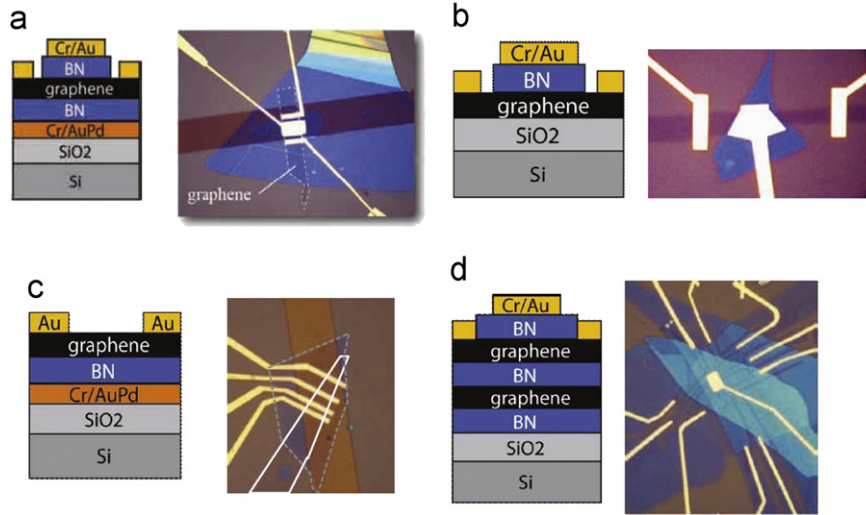


Fig. 10. (Color online) Sample device geometries enabled by the combination of hBN gate dielectrics and the aligned transfer process. (a and b) Dual gated graphene devices for capacitance measurements. (c) Thin hBN FET structure, designed for high transconductance. (d) Dual gated, double layer graphene structure with independence contacts to the two graphene layers. Interlayer Coulomb drag and tunneling measurements are now possible between clean graphene monolayers.

6. Broken symmetry integer and fractional quantum Hall effect in graphene on hBN

The high quality graphene samples made on hBN substrate now allow us to explore the interaction driven symmetry broken quantum Hall states in graphene. Electronic systems with several degenerate degrees of freedom can support a rich variety of broken symmetry states. In 2D, the quantized cyclotron orbits of electron forms highly degenerated Landau levels (LLs), leading to the quantum Hall effect in the extreme quantum condition. At partial filling, exchange interactions can drive the ground state to polarize ferromagnetically [29] within this expanded isospin space, manifesting experimentally as additional integer quantum Hall (QH) plateaus outside the normal sequence. At still higher fields, quantized Hall plateaus appear at fractional LL fillings [30], associated with the formation of a quantum liquid with topological order [31].

In graphene subjected to a quantizing magnetic field, the strong Coulomb interactions and four-fold spin/valley degeneracy lead to an approximate SU(4) isospin symmetry within individual Landau levels. We have performed a series of experiments

devoted to the exploration of these interaction driven quantum Hall states in mono- and bilayer graphenes on hBN substrates.

In the low magnetic field regime, as we presented in the previous section, the observation of a wide number of interaction-induced integer quantum Hall states has been observed. The nature of these broken symmetries can be classified according to their real spin structure *via* tilted field magnetotransport. In particular, at partial filling, exchange interactions can break this symmetry, manifesting as additional Hall plateaus outside the normal integer sequence. Here we report the observation of a number of these quantum Hall isospin ferromagnetic (QHIFM) states, which we classify according to their real spin structure using tilted field magnetotransport. The large activation gaps confirm the Coulomb origin of all the broken symmetry states, but the order depends strongly on LL index. In the high energy LLs, the Zeeman effect is the dominant aligning field, leading to real spin ferromagnets hosting Skyrmonic excitations at half filling, whereas in the ‘relativistic’ zero LL, lattice scale interactions drive the system to a density wave.

Through activation gap measurements, we find evidence for real spin polarized states supporting Skyrmonic excitations,

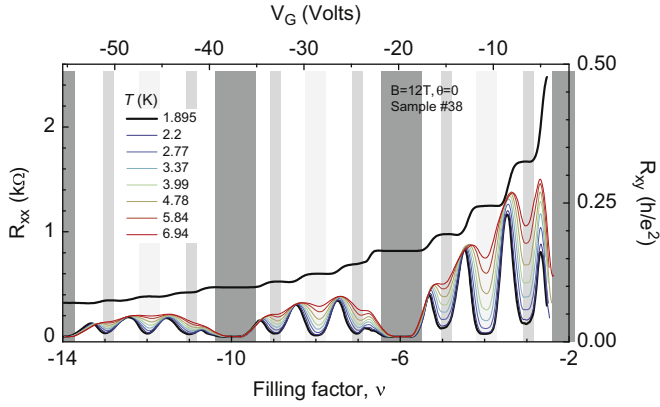


Fig. 11. (Color online) All integer quantum Hall effect in graphene on hBN at different temperatures. R_{xx} minima for different categories of IQH states show clear activation behaviors.

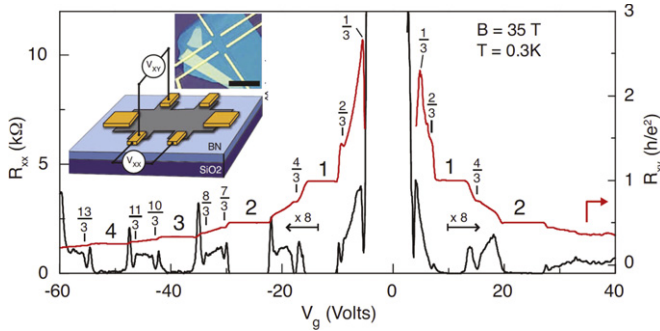


Fig. 12. (Color online) All integer quantum Hall effect in graphene on hBN. Magnetoresistance (left axis) and Hall resistance (right axis) versus gate voltage acquired at $B=35$ T. Inset shows schematic of the etched Hall bar device. Inset: optical image; scale bar is 5 μm .

charge- or spin-density order, and valley textured excitations at different filling factors, revealing the absence of a universally dominant anisotropy in the graphene QHMF (Fig. 11).

In the extreme quantum limit where the Coulomb energy $E_C = e^2/\epsilon\ell_B$ becomes the dominant energy scales, 2D electron systems develop the fractional quantum Hall effect (FQHE) [32]. The FQHE in an electron gas with multiple internal degrees of freedom provides a model system to study the interplay between spontaneous symmetry breaking and emergent topological order [30]. The $SU(4)$ symmetry in graphene discussed above modifies the FQHE and is conjectured to produce new incompressible ground states in graphene [33–36,38–43]. Using high quality graphene on hBN substrate, we performed multiterminal measurements of the FQHE in high mobility graphene [44]. The measured energy gaps are large, particularly in the second Landau level where they measure up to 10 times larger than those reported in the cleanest conventional systems. In the lowest Landau level the hierarchy of FQH states reflects the additional valley degeneracy.

In Fig. 12 the magnetoresistance and Hall conductivity in the FQHE regime of the $n=0$ and $n=1$ LLs are shown. For clarity, the Hall conductivity, calculated from the tensor relation $\sigma_{xy} = R_{xy}/(R_{xx}^2 + (w/l)R_{xx}^2)$, is shown where w/l is the aspect ratio of the Hall bar. We observe the hallmark features of the FQHE, namely quantization of R_{xy} to values of $(1/\nu)h/e^2$ concomitant with minima in R_{xx} , at fractional filling factors $\nu = \frac{1}{3}, \frac{2}{3}$ and $\frac{4}{3}$ in the $n=0$ LL and at $\nu = \frac{7}{3}, \frac{8}{3}, \frac{10}{3}, \frac{11}{3}$ and $\frac{13}{3}$ in the $n=1$ LL. Additionally, a weak minimum in R_{xx} at $\nu = \frac{8}{5}$ is suggestive of an emerging FQHE state at this filling. With the exception of the $\frac{1}{3}, \frac{2}{3}$ and $\frac{4}{3}$, all observed Hall conductivity plateaus are within 1% of their

expected value. At $\frac{1}{3}$ and $\frac{2}{3}$, the Hall plateaus are “N” shaped and do not exhibit exact quantization, typical of FQH states not yet fully formed in magnetic field. The weak formation of the $\frac{1}{3}$ and $\frac{2}{3}$ states may be related to the presence of a competing, insulating phase at low density [45]. Here the appearance of the $\frac{1}{3}, \frac{2}{3}$, and $\frac{4}{3}$ together with the absence of the $\frac{5}{3}$ is consistent with the scenario where symmetry breaking terms remain sufficiently small that an approximate $SU(4)$ symmetry is preserved. We note that previously studied multicomponent 2DES’s such as AIAs and strained silicon [46], in addition to the differences in the orbital character of the wavefunctions, differ from graphene in that the larger ratio between Zeeman and Coulomb energies effectively freezes out the spin degree of freedom at large magnetic fields.

7. Summary

In this paper, we reviewed recently developed a novel technique for substrate engineering of graphene devices using hBN as layered dielectric material to construct vertical heterostructures. We describe the fabrication and characterization of high-quality exfoliated graphene devices on single-crystal hBN substrates employing a mechanical co-lamination and transfer process. Graphene devices on hBN substrates have mobilities and carrier inhomogeneities that are almost an order of magnitude better than devices on SiO_2 . The ability to assemble crystalline layered materials allows us to fabricate more complex graphene based heterostructures. We use the enhanced mobility of electrons in hBN supported graphene to investigate the effects of electronic interactions, where a variety of non-trivial integer and fractional quantum Hall states were observed.

Acknowledgments

This work is supported by DARPA CERA, AFOSR MURI, FCRP through C2S2 and FENA and DOE (DE-FG02-05ER46215).

References

- [1] T. Ando, J. Phys. Soc. Jpn. 75 (2006) 074716.
- [2] M. Ishigami, J.H. Chen, W.G. Cullen, M.S. Fuhrer, E.D. Williams, Nano Lett. 7 (2007) 1643.
- [3] S.V. Morozov, K.S. Novoselov, M.I. Katsnelson, F. Schedin, D.C. Elias, J.A. Jaszczak, A.K. Geim, Phys. Rev. Lett. 100 (2008) 016602.
- [4] S. Fratini, F. Guinea, Phys. Rev. B 77 (2008) 195415.
- [5] J.-H. Chen, C. Jang, S. Xiao, M. Ishigami, M.S. Fuhrer, Nat. Nano 3 (2008) 206.
- [6] E.H. Hwang, S. Adam, S. Das Sarma, Phys. Rev. Lett. 98 (2007) 186806.
- [7] S. Adam, E.H. Hwang, V. Galitski, S.D. Sarma, Proc. Natl. Acad. Sci. U.S.A. 104 (2007) 18392.
- [8] J. Martin, N. Akerman, G. Ulbricht, T. Lohmann, J.H. Smet, K. von Klitzing, A. Yacoby, Nat. Phys. 4 (2008) 144.
- [9] K.I. Bolotin, K.J. Sikes, J. Hone, H.L. Stormer, P. Kim, Phys. Rev. Lett. 101 (2008) 096802.
- [10] X. Du, I. Skachko, A. Barker, E.Y. Andrei, Nat. Nano 3 (2008) 491.
- [11] L.A. Ponomarenko, R. Yang, T.M. Mohiuddin, M.I. Katsnelson, K.S. Novoselov, S.V. Morozov, A.A. Zhukov, F. Schedin, E.W. Hill, A.K. Geim, Phys. Rev. Lett. 102 (2009) 206603.
- [12] M. Laikht, B. Krauss, T. Lohmann, U. Zschieschang, H. Klauk, K.v. Klitzing, J.H. Smet, Nano Lett. 10 (2010) 1149.
- [13] K. Watanabe, T. Taniguchi, H. Kanda, Nat. Mater. 3 (2004) 404.
- [14] A.F. Young, C.R. Dean, I. Meric, S. Sorgenfrei, H. Ren, K. Watanabe, T. Taniguchi, J. Hone, K.L. Shepard, P. Kim, arxiv:1004.5556, 2010.
- [15] I. Meric, M.Y. Han, A.F. Young, B. Özyilmaz, P. Kim, K.L. Shepard, Nat. Nanotechnol. 3 (2008) 654.
- [16] F. Schwierz, Nat. Nano 5 (2010) 487.
- [17] T. Taniguchi, K. Watanabe, J. Cryst. Growth 303 (2007) 525.
- [18] P. Blake, E.W. Hill, A.H.C. Neto, K.S. Novoselov, D. Jiang, R. Yang, T.J. Booth, A.K. Geim, Appl. Phys. Lett. 91 (2007) 063124.
- [19] C. Lee, Q. Li, W. Kalb, X.-Z. Liu, H. Berger, R.W. Carpick, J. Hone, Science 328 (2010) 76.

- [22] J. Xue, J. Sanchez-Yamagishi, D. Bulmash, P. Jacquod, A. Deshpande, K. Watanabe, T. Taniguchi, P. Jarillo-Herrero, B.J. LeRoy, *Nat. Mater.* 10 (2011) 282.
- [23] K. Nomura, A.H. MacDonald, *Phys. Rev. Lett.* 98 (2007) 076602.
- [24] X. Hong, K. Zou, J. Zhu, *Phys. Rev. B* 80 (2009) 241415.
- [25] M.I. Katsnelson, A.K. Geim, *Philos. Trans. R. Soc. A* 366 (2007) 195.
- [26] B.E. Feldman, J. Martin, A. Yacoby, *Nat. Phys.* 5 (2009) 889.
- [27] Y. Zhang, Z. Jiang, J.P. Small, M.S. Purewal, Y.-W. Tan, M. Fazlollahi, J.D. Chudow, J.A. Jaszczak, H.L. Stormer, P. Kim, *Phys. Rev. Lett.* 96 (2006) 136806.
- [28] Y. Zhao, P. Cadden-Zimansky, Z. Jiang, P. Kim, *Phys. Rev. Lett.* 104 (2010) 066801.
- [29] S.M. Girvin, *Ecole d'Ete Les Houches*, July 1998, 1999.
- [30] S. Das Sarma, A. Pinczuk, *Perspectives in Quantum Hall Effects: Novel Quantum Liquids in Low Dimensional Semiconductor Heterostructures*, Wiley-VCH, 1997.
- [31] X.-G. Wen, *Adv. Phys.* 44 (1995) 405.
- [32] D.C. Tsui, H.L. Stormer, A.C. Gossard, *Phys. Rev. Lett.* 48 (1982) 1559.
- [33] C. Toke, P.E. Lammert, V.H. Crespi, J.K. Jain, *Phys. Rev. B* 74 (2006) 235417.
- [34] K. Yang, S. Das Sarma, A.H. MacDonald, *Phys. Rev. B* 74 (2006) 075423.
- [35] K. Nomura, A.H. MacDonald, *Phys. Rev. Lett.* 96 (2006) 256602.
- [36] V.M. Apalkov, T. Chakraborty, *Phys. Rev. Lett.* 97 (2010) 126801.
- [38] M.O. Goerbig, N. Regnault, *Phys. Rev. B* 75 (2007) 241405.
- [39] D.V. Khveshchenko, *Phys. Rev. B* 75 (2007) 153405.
- [40] C. Toke, J.K. Jain, *Phys. Rev. B* 75 (2007) 245440.
- [41] N. Shibata, K. Nomura, *Phys. Rev. B* 77 (2008) 235426.
- [42] N. Shibata, K. Nomura, *J. Phys. Soc. Jpn.* 78 (2009) 104708.
- [43] Z. Papic, M.O. Goerbig, N. Regnault, *Phys. Rev. Lett.* 105 (2010) 176802.
- [44] C.R. Dean, A.F. Young, I. Meric, C. Lee, L. Wang, S. Sorgenfrei, K. Watanabe, T. Taniguchi, P. Kim, K.L. Shepard, J. Hone, *Nat. Nanotechnol.* 5 (2010) 722.
- [45] J.G. Checkelsky, L. Li, N.P. Ong, *Phys. Rev. Lett.* 100 (2008) 206801.
- [46] M. Padmanabhan, T. Gokmen, M. Shayegan, *Phys. Rev. B* 81 (2010) 113301.